

See discussions, stats, and author profiles for this publication at: <https://www.researchgate.net/publication/263941249>

Initial Molecular Photocurrent: Nanostructure and Motion of Weakly Bound Charge-Separated State in Organic Photovoltaic Interface

ARTICLE *in* THE JOURNAL OF PHYSICAL CHEMISTRY C · JANUARY 2013

Impact Factor: 4.77 · DOI: 10.1021/jp309421s

CITATIONS

11

READS

19

3 AUTHORS, INCLUDING:



Yasuhiro Kobori

Kobe University

48 PUBLICATIONS 841 CITATIONS

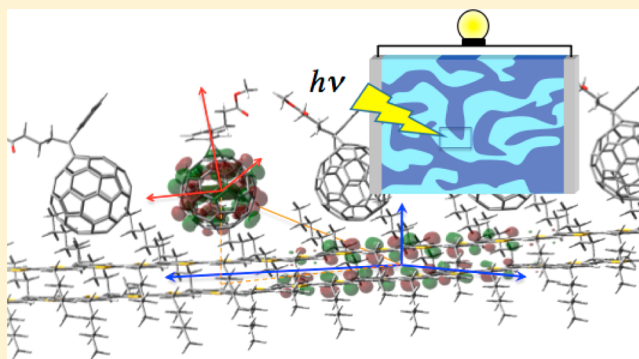
SEE PROFILE

Initial Molecular Photocurrent: Nanostructure and Motion of Weakly Bound Charge-Separated State in Organic Photovoltaic Interface

Yasuhiro Kobori,^{*,†,‡} Ryohei Noji,[†] and Shuhei Tsuganezawa[†][†]Department of Chemistry, Faculty of Science, Shizuoka University, 836 Ohya, Suruga-ku, Shizuoka, 422-8529, Japan[‡]PRESTO, Japan Science and Technology Agency, 4-1-8 Honcho Kawaguchi-shi, Saitama 332-0012, Japan

S Supporting Information

ABSTRACT: To elucidate mechanism of the efficient photo-carrier generation by the photoactive bulkheterojunction layers of the organic photovoltaic (OPV) devices, we have employed the time-resolved electron paramagnetic resonance method on solid blends composed of [6,6]-C₆₁-butyric acid methyl ester (PCBM) and of poly(3-hexylthiophene-2,5-diyl) (P3HT) with different regioregularities. The photoinduced charge-separated (CS) states have been detected at the boundary regions between the P3HT and PCBM domains at $T = 77$ K. We have characterized molecular geometries, electronic couplings, and molecular motions of the long-range CS states. From the CS structure, it is indicated that the pentagonal or hexagonal aromatic rings of the buckyball in PCBM directly face the aromatic plane of the π -stacked P3HT surfaces. It has been concluded that the distant CS states are produced via fast hole-delocalization process from the contact charge-transfer (CT) states. Such hole dynamics is explained by a coupling of the hole to librations of chains in the conjugated polymer. It has been concluded that both the enthalpy stabilization and the enhancement of the entropy occur through the orbital delocalization by the electron–phonon coupling, overcoming the initial CT binding to generate the molecular photocurrent.

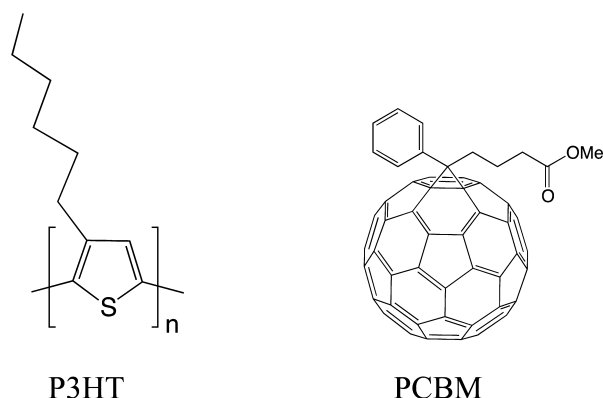


■ INTRODUCTION

Organic bulkheterojunction (BHJ) blend films composed of the conjugated polymers as the electron donors (D) and [6,6]-C₆₁-butyric acid methyl ester (PCBM) as the electron acceptor (A) have been widely known to be useful for the highly efficient photovoltaic device as the organic thin film solar cells.^{1–11} The ultrafast photoinduced charge-injection dynamics has been clarified by the light-excitations of poly(3-hexylthiophene-2,5-diyl) (P3HT) domains in the P3HT:PCBM (Chart 1) blend

films.^{4,12–14} Recent studies have demonstrated that the photoinduced, contact charge-transfer (CT) states are initially generated at the D/A domain-interfaces and play significant roles in the photocurrent generations.^{4,15–17} One of the most puzzling subjects has been that the photocarriers are escaped from the CT binding by the Coulomb attraction, whose energy is several hundreds of millielectronvolts, leading to the photocurrent.^{2,4,7,17} Janssen and coworkers¹⁸ reported that the presence of the nanocrystalline of PCBM with high local carrier mobility accounts for the efficient charge-dissociations; delocalization of the unpaired electron in the PCBM clusters facilitates the reductions of the Coulomb attraction energy.¹⁹ Moreover, morphologies of the P3HT domains are known to be significant for the device performances.^{1,5,20} When the regioregular P3HT (RR-P3HT) in which each monomer unit possesses head-to-tail hexyl configuration is utilized, the polymer chains tend to stack into the planar lamellae structure.^{5,21,22} This structure enhances the interchain hole-mobility^{21,23–26} to contribute to the higher incident photon to current efficiency (IPCE)¹⁰ in the RR-P3HT:PCBM bulkheterojunction solar cells than in the case that the regiorandom P3HT (RRA-P3HT) is adopted, in which the head-to-tail and

Chart 1. Structure Formula of P3HT and PCBM



Received: September 21, 2012

Revised: January 1, 2013

Published: January 2, 2013



the head-to-head hexyl configurations are coexisting.^{12,27} Despite the importance of understanding how the interfaces play roles for the carrier dissociations,^{2,4} no study has experimentally characterized the conformational structure, the electronic interactions, and the motions of the long-range charge-separated (CS) states that can conduct the photocurrents in the OPV systems.

Electron paramagnetic resonance (EPR) spectroscopy has been applied to investigate the characters of the unpaired electronic orbitals because the *g*-tensor of the electron spin, as an example, is the signature of the anisotropy in the magnetic moments²⁸ by the molecular orbitals. The magnetic anisotropies are also very powerful to unveil the conformations of the paramagnetic species.^{29–31} Time-resolved EPR (TREPR) method has been utilized to investigate the short-lived paramagnetic species and their dynamics generated by the nanosecond laser irradiations.^{32–34} The TREPR studies have been reported on the transient CS states generated in the blend materials.^{35–37} However, no geometrical analysis has been performed on the interfacial CS states. In this study, the long-range CS state has been investigated for the solid blend materials of the P3HT:PCBM films with different regioregularities fabricated by solvent annealing procedures. Here we have characterized the unpaired orbital geometries, the electronic couplings, and the molecular motions of the photoinduced CS states at 77 K generated after the initial hole delocalization and dissociation via the contact CT state to clarify the charge dissociation mechanism. From the EPR parameters, it is thermodynamically concluded that the phonon-assisted orbital delocalization play significant roles for overcoming the Coulomb attraction to generate the initial molecular photocurrent.

EXPERIMENTAL SECTION

Samples. RR-P3HT (Aldrich), RRa-P3HT (Aldrich), and PCBM (Tokyo Kasei) were used as received. The homogeneously mixed (1) RR-P3HT/PCBM and (2) RRa-P3HT/PCBM solutions were separately prepared by dissolving P3HT and PCBM with 1:1 (by weight) into 1,2-dichlorobenzene (DCB) (Tokyo Kasei) at 313 K. The freeze–pump–thaw cycles were undertaken to deoxygenate the mixed solutions under the vacuum pressures of 10^{-4} bar using a vacuum line. The solutions were casted at the bottom of the EPR tubes (NES-1, Nihon Seimitsukiki) and at the surface of the quartz cuvettes under the vacuum pressures. From the solutions, solvent was transferred to a round flask using liquid nitrogen to obtain the dry solid films in the quartz tubes for the TREPR measurements and in the quartz cuvettes for the UV–vis spectra at room temperature. The sample tubes and cuvettes were sealed by an oxygen torch, leaving the blend films inside the cells, as shown in the inset of Figure 1. No thermal annealings were undertaken before the measurements.

Time-Resolved EPR. The X-band TREPR measurements were carried out using a Bruker EMX system without using the field modulations. In the microwave bridge, a modified wide-band preamplifier (ER047PH) was equipped. Light excitations were performed by the second harmonics (532 nm) of a Nd:YAG laser (Continuum, Minilite II, fwhm ~ 5 ns). A laser depolarizer (SIGMA KOKI, DEQ 1N) was placed between the laser exit and the microwave cavity for the TREPR experiments. Transient EPR signals were averaged by a digital oscilloscope (Tektronix, TDS 520D) at 201 different external magnetic field positions and were transferred to a personal computer via a

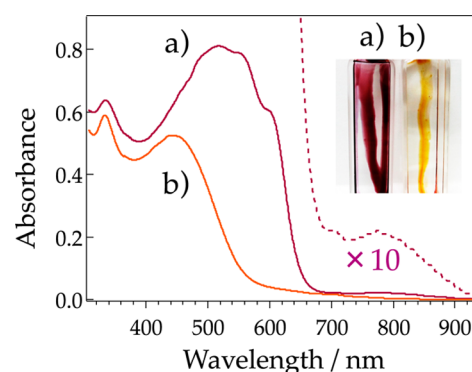


Figure 1. UV–vis absorption spectra of the blend films of (a) 1:1 RR-P3HT:PCBM and (b) 1:1 RRa-P3HT:PCBM fabricated by the solvent annealing of the mixed solutions in 1,2-dichlorobenzene under the vacuum pressures. Dashed line is obtained by expanding the spectrum a in intensity. Inset shows photos of the blend films of a and b in quartz cuvettes.

GPIB communication to obtain the 2-D TREPR data. The sample tubes were placed in a liquid-nitrogen Dewar flask filled with the liquid nitrogen and was fixed inside the EPR cavity. The microwave power was set to be $\omega_1 = 9.5 \times 10^5$ rad/s and is used for the theoretical computation of the transverse magnetization.

RESULTS AND DISCUSSION

Morphologies of the P3HT:PCBM Blend Films. The UV–vis absorption spectra were observed for the 1:1 blend solid films fabricated inside the quartz cuvette, as shown in Figure 1. As for the RR-P3HT:PCBM blend, strong vibrational absorption bands around 530 nm are obtained, which are characteristics of the crystalline phase by the RR-P3HT molecules.⁹ This absorption is overlapping to the shoulder band of the PCBM absorption ranging from 300 to 550 nm,¹⁰ indicating that even though the PCBM molecules are present in the film the interchain lamellae stacking structure is not disrupted in the P3HT domains because of the “solvent annealing”^{9,38} effect by which the RR-P3HT molecules tend to be highly self-organized to form the phase segregation by the P3HT microcrystals. This phase segregation by the crystalline P3HT and by the PCBM domains is known to contribute to the higher IPCE by the 1:1 blend film.^{8,9} The crystalline feature in RR-P3HT is in contrast with the reported morphology of the corresponding blend films obtained by the fast spin-coating procedures exhibiting the broad absorption band around 450 nm, which is due to the disordered RR-P3HT single chains.²⁷ The 450 nm band is seen in the 1:1 RRa-P3HT:PCBM blend film, as shown by the orange line in Figure 1b, denoting that the RRa-P3HT molecules do not form the self-organized structure. In the present RR-P3HT:PCBM blend, the absence of the 450 nm band shows that the conformational chain defects by the inclusion of the PCBM molecules are minor at the interfacial region between the PCBM and P3HT domains. A broad absorption band is obtained around 770 nm in Figure 1 and is assigned to the CT transition of the RR-P3HT/PCBM complex.^{15,39} This result indicates that there exist the π -stacking interactions at the interfaces of the domains.⁴⁰

Time-Resolved EPR Spectra. Figure 2 shows the EPR spectra obtained by the 532 nm laser excitations of the RR-P3HT:PCBM (left) and the RRa-P3HT:PCBM (right) blends detected at $T = 77$ K. In Figure 2, the spectrum e represents the

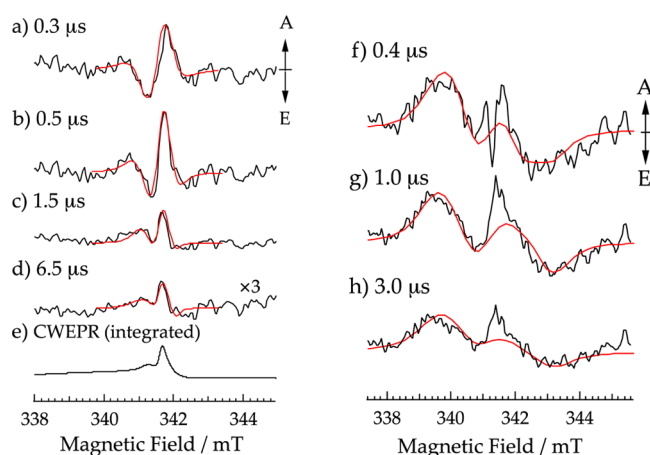


Figure 2. (a–d) TREPR spectra of the RR-P3HT:PCBM blend film obtained at several delay times after the 532 nm laser irradiations at $T = 77$ K. (e) Steady-state EPR spectrum of the RR-P3HT:PCBM blend taken during the photoirradiations after the field integration of the first-derivative signal at 77 K. (f–h) TREPR spectra of the RR-P3HT:PCBM blend at 77 K. Red lines are simulated TREPR spectra of the transverse magnetization in the photoinduced CS states calculated using the stochastic-Liouville equation for the singlet–triplet states in the rotating frame.

integrated form of the first-derivative EPR spectrum obtained by the standard phase-sensitive detection with the field modulation during the continuous laser irradiations of the RR-P3HT:PCBM blend film, whereas the other spectra are the direct-detected TREPR spectra at selected delay times after the 532 nm laser excitations. The spectrum in panel e was explained by the sum of the dissociated polarons generated by the photoinduced carrier-dissociations to yield (1) $\text{P3HT}^{+\bullet}$ for the lower field position ($g = 2.002$) and (2) $\text{PCBM}^{-\bullet}$ for the higher field position ($g = 1.999$).^{28,36,41} Note that in the TREPR measurements the long-lived stable species in Figure 2e accumulated by the continuous light irradiations are filtered by the preamplifier and are thus not detectable. In Figure 2a–d, the resonance field region is close to the resonant magnetic field in Figure 2e but is evidently wider than the dissociated polaron spectra. This result is explained by broadening by the spin–spin dipolar coupling in the radical pair composed of $\text{P3HT}^{+\bullet}$ and $\text{PCBM}^{-\bullet}$ at low temperature; the bound CS state is immediately generated at the interface between the PCBM and P3HT domains by the photoirradiations. In Figure 2, the initial microwave transitions show symmetric A/E/A/E pattern, where A and E denote the microwave absorption and emission, respectively. In the homogeneously mixed RRa-P3HT:PCBM and RR-P3HT:PCBM blend materials, Guo et al. reported that all of the singlet excitons reach the interfaces of the P3HT/PCBM after the light irradiations and then form radical ion pairs within picosecond time scales.¹² Also, such ultrafast charge-generation dynamics are reported to be temperature-independent,¹⁴ indicating that the singlet radical ion pairs are predominantly generated in the present blend materials. Therefore, the initial A/E/A/E electron spin polarizations (ESPs) in Figure 2 originate from the singlet precursor, spin-correlated radical pairs (SCRPs).^{29,42} Because the broadenings by the spin dipolar coupling are evident on the TREPR spectra in Figure 2, the A/E/A/E polarization patterns need to be analyzed (vide infra) using a combination of the anisotropic magnetic interactions of the spin-dipolar coupling and the Zeemann interaction (g -anisotropy), as has been considered for

the SCRPs in the photosynthetic reaction centers.^{29,30,32,43,44} Recent studies have shown that the efficient photoinduced charge-generation takes place via the CT complexes in the P3HT:PCBM systems.^{4,15–17} The observations of the CT absorption band and the dominant crystalline feature in the P3HT domain (Figure 1a) imply that the bound CS state in Figure 2a originates from structurally defined P3HT-PCBM complexes formed by the π -stacking interactions at the interfaces. At the left side of Figure 2, the A/E/A/E pattern changes to the absorptive polarization in Figure 2c,d. This is explained by the spin–lattice relaxation to generate the thermal equilibrium spin populations in the spin states of the SCRP.^{31,36}

Figure 3 shows the time profile of the TREPR signal at the field of $B_0 = 341.2$ mT in the RR-P3HT:PCBM system at $T =$

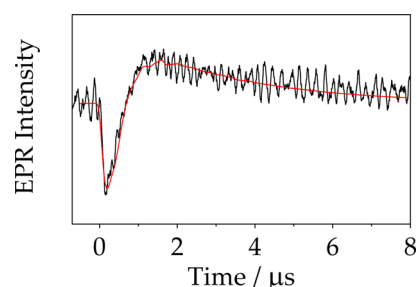


Figure 3. Time profile of the TREPR signal obtained at 341.2 mT in the RR-P3HT:PCBM system (Figure 2 left) at 77 K. Red line is calculated profile of eq 4 using the SLE at the selected field of 341.2 mT. $\theta = 60^\circ$, $\phi = 32^\circ$, $\alpha = 0^\circ$, $\beta = 18^\circ$, $\gamma = 0^\circ$ and $J = 8$ μT are employed for the computation of the transverse magnetization with $D = -0.42$ mT.

77 K. The quick rise (~ 100 ns) in the initial emissive signal is governed by the time resolution of the spectrometer and is consistent with the reported fast charge-generation dynamics described above. The quick rise in the signal also denotes that the transverse relaxation time (T_2) is as fast as nanosecond region in the SCRP. The decay of the initial emissive component is in line with the spectrum change to the absorptive thermal equilibrium signal in Figure 2b,c, corresponding to the spin–lattice relaxation of the SCRP. The decay of the absorptive signals in Figure 3 is dominated by a single exponential function with a lifetime of a few microseconds. This decay is thus explained by the geminate charge-recombination (CR) of the bound CS state, indicating that the majority of the radical pair state is deactivated within a few microseconds at 77 K. This result is consistent with the reported first-order decay of the microwave photoconductance dominated by the geminate CR process at lower temperature.¹⁴ Also, in the solar-cell device employing the RR-P3HT:PCBM film, it has been reported that the photocurrent density (J_{SC}) at the voltage of 0 V highly decreased by more than an order of magnitude when the temperature was reduced from 300 to 77 K.¹⁵ This result is reasonably explained by the predominant losses of the electrons and the holes by the geminate CR at the lower temperature ($T < 100$ K) and is coincident with the present microsecond decay of the SCRP. The predominant single-exponential decay of the thermal equilibrium signal in Figure 3 thus indicates that the observed SCRP signals are dominated by the radical-pairs $\text{D}^{+\bullet}/\text{A}^{-\bullet}$ with similar electronic couplings (V_{CR}) for the CR at the solid interfaces, suggesting that the origin of the E/A/E/A pattern is the CS states of $\text{P3HT}^{+\bullet}$ – $\text{PCBM}^{-\bullet}$ with similar molecular geometries. The kinetic

properties of the spin-relaxations and of the CR are reasonably obtained by a theoretical simulation of the transverse magnetization (red line in Figure 3, as detailed in the following section) of the CS state with analyzing the stochastic-Liouville equation in the rotating frame, taking into account the experimental microwave field strength described above.

In the RRA-P3HT:PCBM system (Figure 2 right), both of the broad components and the sharp signals are observed, indicating that the distances between the unpaired electrons are inhomogeneous in the photoinduced CS states. As for the broad EPR components, the spectrum width in the RRA-P3HT:PCBM is much larger than the width in the RR-P3HT:PCBM, denoting that the shorter-range CS states are dominantly generated in the RRA-P3HT:PCBM film in which no P3HT's self-organization is present, as seen by the lack of the P3HT exciton band in Figure 1b. The sharp component in Figure 2f exhibits an A/E/A polarization pattern. This polarization would be explained by the SCR model as a distant CS state. The A/E/A polarization quickly changes to the absorptive signals in Figure 2g,h, those of which are explained by the thermal equilibrium populations by the spin-lattice relaxation, as detected in the RR-P3HT:PCBM system in Figure 2c,d. Because these center components are not well-resolved and minor, we did not undertake any analysis in the present study.

It is noticeable that the 532 nm light irradiations of the RR-P3HT:PCBM blend selectively produce the excited singlet states of the delocalized P3HT exciton ($^1\text{RR-P3HT}^*$) due to the dominant microcrystalline feature around the 530 nm absorption (Figure 1a) of the RR-P3HT domain; the singlet CS states in Figure 2a–d are generated after the efficient excitation migrations in the P3HT lamellae structures to the boundaries between the D/A domains, as has been reported by Ohkita and his coworkers.¹² This fact denotes that the holes of $\text{P3HT}^{+\bullet}$ in the singlet CS state are located at the crystalline RR-P3HT region of the domain-boundaries, where the hole mobility is greater than the mobility in the disordered RRA-P3HT.¹² The charge mobility of $\text{PCBM}^{-\bullet}$ is much smaller at 77 K than the mobility of $\text{P3HT}^{+\bullet}$ in the RR-P3HT:PCBM blend.¹⁴ The larger separation distance of the CS state in the RR-P3HT:PCBM blend than in the RRA-P3HT:PCBM is thus interpreted by the initial interchain hole delocalization⁴⁵ and the trapping by the localized $\text{PCBM}^{-\bullet}$ due to the weak Coulomb attraction. Similar delocalized CS states are reported in the DNA hairpin systems,⁴⁶ where an excited perylenediimide (P) molecule incorporated in the hairpin injects the hole into the π -stacked adenine (A) bases to form the CS state with a polaron ($\text{A}_{3-4}^{+\bullet}$) delocalized in 3–4 bases at a 1.4 nm distance from the radical anion, $\text{P}^{-\bullet}$. As for the broader TREPR spectra in the RRA-P3HT:PCBM system, the shorter separation distance of the CS state is explained by a more localized hole distribution in the single P3HT-chain due to the lack of the organized crystalline region. From the width of the spectra, the dipolar coupling constant is estimated to be -2 mT. By using the simple point-dipole approximation, the center-to-center distance (r_{CC}) in the CS state is estimated to be 1.1 nm. Because this separation is too distant as the charge-transfer complex, the observed CS state is explained by an intrachain hole dissociation in the vicinity of the $\text{PCBM}^{-\bullet}$ molecule after the initial ultrafast photoinduced electron-transfer¹² in the CT complex.

Analysis of the Time-Resolved EPR Data. To obtain the detailed structural and electronic properties of the transient CS

states, we have performed the analyses of the TREPR data on the basis of the stochastic-Liouville equation (SLE),⁴⁷ in which the time-dependent quantum mechanical phenomena starting from the singlet are considered for the density matrix ($\hat{\rho}$) in the rotating frame on the basis spin-functions of $|+\rangle = |\alpha\alpha\rangle$, $|0\rangle = |\alpha\beta + \beta\alpha\rangle/\sqrt{2}$, $|-\rangle = |\beta\beta\rangle$ for the triplet CS state, and $|S\rangle = |\alpha\beta - \beta\alpha\rangle/\sqrt{2}$ for the singlet CS state, as follows,

$$\frac{\partial \hat{\rho}}{\partial t} = -i[\hat{H}_{\text{RP}}^r, \hat{\rho}] - \mathbf{K}\hat{\rho} - \mathbf{W}\hat{\rho} \quad (1)$$

where \hat{H}_{RP}^r is the spin Hamiltonian including the interactions of the electron spin angular momentum \mathbf{S} with the microwave as

$$\hat{H}_{\text{RP}}^r = \hat{H}_0 - \omega_0 \hat{S}_z + \omega_1 \hat{S}_x \quad (2)$$

where ω_0 and ω_1 are the microwave frequency and the microwave field strength, respectively. The spin Hamiltonian H_0 in the radical pair is composed of Zeeman interaction, hyperfine interactions, the spin–spin exchange coupling, and the spin-dipolar coupling as

$$\begin{aligned} \hat{H}_0 = & \beta B_0 \{g_1(\mathbf{\Omega})\hat{S}_1 + g_2(\mathbf{\Omega})\hat{S}_2\} + \sum_i A_{1,i}(\mathbf{\Omega})\hat{S}_1\hat{I}_{1,i} \\ & + \sum_j A_{2,j}(\mathbf{\Omega})\hat{S}_2\hat{I}_{2,j} - 2J\left(\frac{1}{2} + \hat{S}_1\hat{S}_2\right) + \hat{\mathbf{S}}\mathbf{D}(\mathbf{\Omega})\hat{\mathbf{S}} \end{aligned} \quad (3)$$

where $\mathbf{\Omega}$ denotes the direction of the external magnetic field. In eq 3, the hyperfine couplings of the $\text{PCBM}^{-\bullet}$ (radical 1) are negligibly small and are ignored in the present analysis. The time-dependent EPR signal of $EPR(t)$ is represented as the transverse magnetization, as follows⁴⁴

$$EPR(t) = \text{Tr}\{\hat{S}_y \hat{\rho}(t)\} \quad (4)$$

In eq 1, the effects of the spin relaxations (\mathbf{W} : as determined by spin–lattice relaxation time of T_1 and the transverse relaxation time of T_2) and the CR kinetics \mathbf{K} are taken into account in the 16×16 matrix form of eq 1 on the basis spin functions of $|+\rangle$, $|0\rangle$, $|-\rangle$, and $|S\rangle$ for the CS states. The matrix form is detailed in the Supporting Information. In the spin Hamiltonian, the anisotropies of the Zeeman interaction, the spin–spin dipolar interaction (\mathbf{D}), and the hyperfine interactions in $\text{P3HT}^{+\bullet}$ are considered, whereas the singlet–triplet electronic energy gap (exchange coupling: $2J$) has been treated to be isotropic. Figure 4 shows the g -tensor orientations (g_x , g_y , and g_z for $\text{P3HT}^{+\bullet}$ and g_x , g_y , and g_z for $\text{PCBM}^{-\bullet}$) and the dipolar principal axis (dashed arrow) depicted on the CS state in the D–A molecular complex at the interface. In this study, the position of the $\text{PCBM}^{-\bullet}$ is set by the polar angles (θ and ϕ) with respect to the principal g axes of $\text{P3HT}^{+\bullet}$ (Figure 4a). Orientation of the principal g -axes in $\text{PCBM}^{-\bullet}$ is considered by using the Euler angles of α , β , and γ (Figure 4b) with respect to the principal g -axes in $\text{P3HT}^{+\bullet}$. The principal values of the g -tensors²⁸ are listed in Table 1 for $\text{P3HT}^{+\bullet}$ and $\text{PCBM}^{-\bullet}$.

Axes Setting of the g -Tensors. For the computations of the TREPR spectra to determine the molecular geometries of the CS states, the principal axes and values of the g -tensors are defined as follows. Orientation dependence on the EPR spectrum of the organic field-effect transistor (FET) of ultrathin RR-P3HT layers has determined that the g -factor of $\text{P3HT}^{+\bullet}$ is smallest for the chain direction and is largest for the short-axis direction in the aromatic plane.⁴⁸ Thus, from the

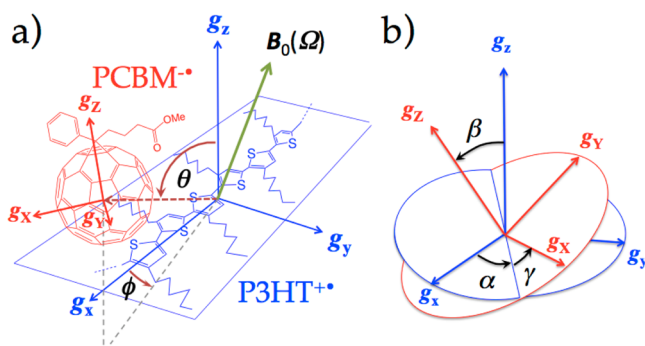


Figure 4. (a) Angle settings for the $\text{PCBM}^{\bullet-}$ position in the weakly bound CS state at the photovoltaic interface of the BHJ films considered for the computations of the TREPR spectra (red lines in Figure 2). In $\text{PCBM}^{\bullet-}$, the directions of g_X and g_Y are not clear in the equatorial X – Y plane bisecting the C_{60} sphere but are assumed in the present study to be parallel and perpendicular, respectively, to the 6–6 ring bond at the top of C_{60} . (b) Orientation of $\text{PCBM}^{\bullet-}$ represented by the red principal axis system, which is defined by the Euler angles of α , β , and γ with respect to the principal axes (blue arrows) of the g -tensor in $\text{P3HT}^{\bullet+}$. Because $g_X \approx g_Y$ in $\text{PCBM}^{\bullet-}$, the effects of the α and γ angles cannot be exactly distinguished.

reported g -factors in the RR-P3HT:PCBM blend using a high-field EPR spectroscopy,²⁸ $g_x = 2.00110$, $g_y = 2.00380$, and $g_z = 2.00230$ can be set for $\text{P3HT}^{\bullet+}$ in Figure 4a. In $\text{PCBM}^{\bullet-}$, the principal values are reported at cryogenic temperature to be $g_X = 2.00058$, $g_Y = 2.00045$, and $g_Z = 1.99845$.²⁸ These principal values are similar to $g_X = 2.00085$, $g_Y = 2.00038$, and $g_Z = 1.99925$ obtained for radical anion of N -methyl-3,4-fulleropyrrolidine (MFP) in which one dimethylamino group is bridged at the same 6–6 ring bond (referred here as the top of C_{60}) as the substituent of $\text{PCBM}^{\bullet-}$.⁴⁹ From the hyperfine couplings of the radical anion of MFP, the spin density distribution was coincident with the lowest unoccupied molecular orbital (LUMO) in MFP where the electron density is mostly distributed in the vicinity of the equatorial X – Y plane bisecting the C_{60} sphere rather than in the vicinity of the top direction axis.⁴⁹ Taking into account the equatorial distribution of the LUMO⁵⁰ and $g_X \approx g_Y$ in $\text{PCBM}^{\bullet-}$, one can deduce that the g_Z axis is the top direction in C_{60} , whereas g_X and g_Y axes are in the equatorial plane, as shown in Figure 4a. Because of $g_X \approx g_Y$ in $\text{PCBM}^{\bullet-}$, direction assignments of the g_X and g_Y axes are not clear. Here the g_X axis is assumed to be parallel to the 6–6 ring bond direction, as depicted in Figure 4a. Because of the

symmetrical equivalences in the magnetic interactions by the dipolar coupling and the g -tensor, eight-fold geometries are possible to reproduce the TREPR data.⁴³ Thus, in the present computations, we have first restricted the angle parameters for the spin-dipolar coupling and for the g -tensor orientation to be $0 \leq \theta \leq \pi/2$, $0 \leq \phi \leq \pi/2$, $-\pi/2 \leq \alpha \leq \pi/2$, $-\pi/2 \leq \beta \leq \pi/2$, and $-\pi/2 \leq \gamma \leq \pi/2$ in Figure 4.

Nanostructure of the Transient CS States. To reproduce the TREPR spectra in Figure 2, we have directly computed the transverse magnetization of eq 4 (as detailed in the Supporting Information) as a function of the external magnetic field at the corresponding delay times t in Figure 2. Also, eq 4 has been computed as a function of t to fit the time profile in Figure 3. For the computations, a response time (150 ns) of the spectrometer has been considered by a single exponential function to convolute the time-dependent EPR signals. Because the EPR transitions by the thermal equilibrium spin polarizations ($P_{\text{eq}} = g\beta B_0/2k_B T$) are observed as the absorptive signals for $t > 1 \mu\text{s}$, as shown in Figure 3, one can now quantitatively evaluate the initial ESP magnitudes⁴³ with respect to P_{eq} in the SCR by using eq 4. Previous TREPR investigation⁵¹ has shown that the initial ESP magnitude is highly sensitive to the size of the exchange coupling of $2J$. In the present calculations, when one set $J > 20 \mu\text{T}$ for the RR-P3HT:PCBM system, E/A-polarized spectra were always calculated at $t = 0.3$ and $0.5 \mu\text{s}$ and were highly deviated from the A/E/A/E ESP in Figure 2a for any combinations of θ , ϕ , α , β , and γ . Also, the calculated initial ESP magnitudes are much larger than P_{eq} and thereby do not reproduce the time profile at $B_0 = 341.2 \text{ mT}$ in Figure 3. When $J < 2 \mu\text{T}$ is considered, one is again unable to find any combination of the angle parameters to reproduce the A/E/A/E shape in Figure 2a,b under the given g -tensor components and directions in Table 1 and in Figure 4a. We find that the TREPR spectra of Figure 2a,b and the time profile in Figure 3 are all reproduced as shown by red lines in Figure 2a,b and 3 with a common set of the five angle-parameters ($\theta = 60^\circ$, $\phi = 32^\circ$, $\alpha = 0^\circ$, $\beta = 18^\circ$, and an arbitrary value in γ , as referred here as Conformation I) under $J = 8 \mu\text{T}$, taking into account the spin relaxation parameters of $T_1 = 0.5 \mu\text{s}$ and $T_2 = 12$ – 15 ns with $k_{\text{CRT}} = 4.2 \times 10^5 \text{ s}^{-1}$ as the CR rate constant from the triplet CS state.¹⁷ Even for the absorptive TREPR spectrum for $t = 1.5 \mu\text{s}$, the spectrum shape was well-reproduced (as shown by the red line in Figure 2c) by using $J = 8 \mu\text{T}$ with the slight differences in the five angles ($\theta = 64^\circ$, $\phi = 30^\circ$, $\alpha = 5^\circ$, $\beta = 18^\circ$, and an arbitrary value

Table 1. Parameters for Simulations of the Time-Dependent EPR Spectra of the Photoinduced CS States in the 1:1 P3HT:PCBM Blend Films at 77 K

blend films	D/mT^a	$J/\mu\text{T}^b$	$k_{\text{CRT}}/10^5 \text{ s}^{-1c}$	$T_1/\mu\text{s},^d T_2/\text{ns}^e$	dipolar angles ^f	Euler angles ^f	principal g -tensor components	
							P3HT ^{•+}	PCBM ^{•-}
RR-P3HT:PCBM	−0.42	8	4.2	0.50 15	$\theta = 60^\circ$ $\phi = 32^\circ$	$\alpha = 0^\circ$	$g_x = 2.00110$	$g_x = 2.00058$
						$\beta = 18^\circ$	$g_y = 2.00380$	$g_y = 2.00045$
						γ : arbitrary	$g_z = 2.00230$	$g_z = 1.99845$
RRa-P3HT:PCBM	−2.2	28	14	0.70 9	$\theta = 75^\circ$ $\phi = 15^\circ$	$\alpha = 0^\circ$		
						$\beta = 18^\circ$		
						γ : arbitrary		

^aSpin–spin dipolar coupling between $\text{P3HT}^{\bullet+}$ and $\text{PCBM}^{\bullet-}$. ^bSpin–spin exchange coupling between $\text{P3HT}^{\bullet+}$ and $\text{PCBM}^{\bullet-}$. Fitting errors are $\pm 0.5 \mu\text{T}$. ^cCharge-recombination rate constant from the triplet CS state to the excited triplet P3HT. ^dSpin–lattice relaxation time. ^ePhase memory time for the transverse magnetization. ^fFitting errors are $\pm 2^\circ$. In RR-P3HT:PCBM blend, the parameters of Conformation I are listed and are used for the views of the structures in Figure 5 and 6. Several alternative combinations of $(\alpha, \beta) = (-90^\circ, 20^\circ), (-45^\circ, 18^\circ), (45^\circ, -18^\circ),$ and $(90^\circ, -20^\circ)$, as examples, well reproduce the TREPR data both for the RR-P3HT:PCBM and for the RRa-P3HT:PCBM.

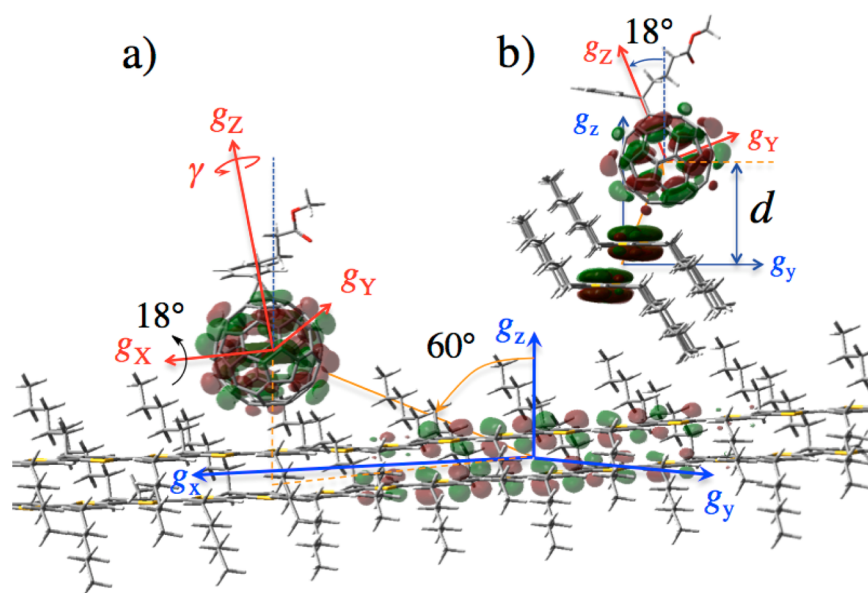


Figure 5. One of the geometries to reproduce the TREPR spectra for the unpaired electron orbitals in the photoinduced CS state at the D–A interface of the RR-P3HT:PCBM BHJ film generated by the light excitation of the crystalline phase of the P3HT domain at 77 K (Conformation I). (a) In this view, $\theta = 60^\circ$ and $\beta = 18^\circ$ in Table 1 are shown for the position and the orientation of PCBM $^{\bullet-}$, respectively. To fit the TREPR data, the angles of α and γ can be treated to be arbitrarily distributed for the rotations of PCBM $^{\bullet-}$ about the g_z axis. (b) View from the long-axis of the P3HT chains. $\beta = 18^\circ$ denotes that the hexagonal aromatic ring at the PCBM bottom faces the aromatic plane of P3HT, giving rise to the π -stacking interaction between PCBM and P3HT to contribute to the CT transition and to the efficient electron injection from $^1\text{P3HT}^*$ to PCBM. The height (d) from the g_x – g_y plane to the center of the buckyball is obtained to be $d = 0.88$ nm, resulting in $r_{\text{CC}} = 1.8$ nm in panel a between the centers of the unpaired electronic orbitals.

in γ) from Conformation I. Furthermore, under $J = 8 \mu\text{T}$ with $\theta = 60^\circ$, $\phi = 32^\circ$, and an arbitrary value in γ , we have obtained several combinations of the angles of $(\alpha, \beta) = (-90^\circ, 20^\circ)$, $(-45^\circ, 18^\circ)$, $(45^\circ, -18^\circ)$, and $(90^\circ, -20^\circ)$, as examples to reproduce the TREPR data. When we have considered $J = 4 \mu\text{T}$, several sets of the five angle-parameters ($\theta = 37^\circ$, $\phi = 40^\circ$, $\beta = 90^\circ$, and arbitrary values in α and γ) are found to reproduce the shapes of the TREPR data in Figure 2a, 2b and Figure 3. However, TREPR spectrum at $t = 1.5 \mu\text{s}$ was not well reproduced using these parameters. When $J = 2.5 \mu\text{T}$ is adopted, both of the spectrum shapes in Figure 2a and 2b are reproduced with the other set of the five angles ($\theta = 18^\circ$, $\phi = 90^\circ$, $\alpha = 0^\circ$, $\beta = 50^\circ$ and an arbitrary value in γ). However, with this parameter set, the calculated time-profile in Figure 3 is not well reproduced. As a result, it has been found that $J = 8 (\pm 0.5) \mu\text{T}$ provides the convincing best-fit calculations as shown by the red lines in the left of Figure 2 and in Figure 3 using the several common sets of the five-angle parameters as described above for the RR-P3HT:PCBM system.

The exchange coupling of $J = 8 \mu\text{T}$ has been revealed to be consistent with the electronic coupling for the triplet CR kinetics, as detailed in the following section. Therefore, we conclude that the combinations of ($\theta = 60^\circ$, $\phi = 32^\circ$, and $\beta = \pm 18$ – 20°) are the angle parameter sets to represent the conformations of the transient CS states in the RR-P3HT:PCBM system at 77 K. In the present calculation, because $g_x \approx g_y$, the angles of α and γ cannot be distinguished for the rotations of the PCBM $^{\bullet-}$ molecule about the g_z axis. There may still exist the other sets^{43,52,53} of the angles (θ , ϕ , α , and β) to reproduce the time dependence of the EPR (Figures 2a–c and 3) for the RR-P3HT:PCBM system. Consistencies of the calculated angle parameters with the RR-P3HT-PCBM molecular complex are discussed below. With the similar calculation procedures (as shown by red lines in Figure 2f–g),

the EPR parameters for the RRa-P3HT:PCBM system are also obtained. Table 1 summarizes the parameters for the SLE calculations to fit the TREPR spectra both for the RR-P3HT:PCBM and the RRa-P3HT:PCBM.

Under the given g -tensor components and directions in Table 1 and in Figure 4a, the spectrum pattern is revealed to be highly sensitive to the dipolar angles of θ and ϕ ; when $\theta = 0^\circ$ is set, the E/A/E/A pattern, which is totally inverted phase from the A/E/A/E in Figure 2a, is predicted as shown in Figure S1 of the Supporting Information, whereas $\theta = 60^\circ$ in Conformation I yields the A/E/A/E pattern that is very close to the experimental results in Figure 2a. This is due to a combination of the different anisotropic effects: the electron spin dipolar interaction and the Zeeman interaction. β in Figure 4b corresponds to the angle between the out-of-plane direction of P3HT and the top (g_z) direction of the PCBM molecule. This tilt angle also strongly affects the spectrum shape, whereas the γ angle does not largely contribute to the shape. This is because the g_z value in PCBM is extremely smaller than g_x and g_y and $g_x \approx g_y$. Thus, $\beta = \pm 18$ – 20° is essential as well to reproduce the observed EPR spectra (red lines) in Figure 2. $\beta = \pm 18$ – 20° implies that the hexagonal or pentagonal aromatic ring at the PCBM bottom faces the aromatic plane of P3HT, giving rise to the strong π -stacking interactions with the P3HT surface, as shown in Figure 5b. This is compatible with the CT transition band⁴⁰ in Figure 1 and with the reported model structures of the P3HT/PCBM CT complexes.^{4,13,15} From the EPR parameters and the anticipated hole delocalization⁴⁵ in the RR-P3HT lamellae structure,^{22,24} one of the nanostructures of the CS states is derived for the Conformation I in the RR-P3HT:PCBM as, shown in Figure 5. The structure of the P3HT region is based on a recent electron diffraction analysis that has revealed a tilted packing structure with short π – π stacking of a 0.34 nm interplanar distance.^{22,54} The interchain

delocalized hole distribution is consistent with the dimer polaron model, which explains the absorption spectra for the polarons reported in the 2D-lamellae regions.⁴⁵ In Figure 5, the PCBM^{•-} orientation obeys $\alpha = 0^\circ$ and $\gamma = 0^\circ$, showing that one hexagonal aromatic ring at the PCBM bottom faces the aromatic plane of P3HT, as shown in Figure 5b. Because $g_x \approx g_y$ in PCBM^{•-}, the situation of $\alpha = 0^\circ$ and $\gamma = 90^\circ$ also reproduces the TREPR data in Figure 2 as an example. Therefore, the pentagonal aromatic ring at the PCBM bottom may also face the P3HT plane. In the BHJ film, it is strongly anticipated that the PCBM molecular conformations are in amorphous environment at the domain boundaries so that the α and γ angles will be arbitrarily distributed at the D/A interfaces. It should be noted that even if the α and γ angles are randomly oriented, the hexagonal and/or pentagonal rings tend to face to the P3HT planes at the interfaces, giving rise to the strong π -stacking interactions between PCBM and P3HT. These aromatic stacking situations can explain the efficient electron injection dynamics from ¹P3HT* to PCBM, as described above. In Figure 5b, a height (d) is determined to be $d = 0.88$ nm from the g_x - g_y plane to the center position of the C₆₀ sphere by summing the 0.17 nm height (= half of the 0.34 nm interplanar stacking distance²² in the P3HT lamellae), the reported edge-to-edge stacking distance (0.35 nm)¹³ between the P3HT and PCBM molecules, and the radius (0.36 nm) of the C₆₀ sphere. From $\theta = 60^\circ$, the center-to-center distance (r_{CC}) between the unpaired orbitals is obtained to be $r_{CC} = d/\cos \theta = 1.8$ nm for the orange straight line in Figure 5a. From the simple point-dipole approximation, $r_{CC} = 1.8$ nm gives the spin dipolar coupling of $D = -0.47$ mT.³⁴ Considering the interchain delocalized hole distribution in Figure 5 to weaken the dipolar interaction, $r_{CC} = 1.8$ nm is a reasonable center separation to provide $D = -0.42$ mT for the long-range CS state in Table 1. Thereby, the parameters in Table 1 self-consistently explain the nanostructure of Figure 5. Additionally, because no steric hindrances are seen between the PCBM molecule and the P3HT self-organization structure in Figure 5, the proposed CS structure originating from the π - π stacking interactions is valid for any γ angle. Instead of Conformation I shown in Figure 5, the alternative conformations of $(\alpha, \beta) = (-90^\circ, 20^\circ)$, $(-45^\circ, 18^\circ)$, $(45^\circ, -18^\circ)$, and $(90^\circ, -20^\circ)$ well-reproduced the TREPR data. These geometries also exhibit no steric hindrances between the PCBM molecule and the P3HT structure from Figures 4 and 5 for any γ , representing the validities of the interfacial CS structures generated by the strong π -stacking interactions between PCBM and P3HT. On the contrary, for the smaller J values, the several other sets of the angle parameters of $(\theta = 37^\circ, \phi = 40^\circ, \beta = 90^\circ)$ and $(\theta = 18^\circ, \phi = 90^\circ, \beta = 50^\circ)$ are found to reproduce the TREPR data, as described above. However the larger angles in β will not produce the predicted strong π - π stacking structure, generating highly hindered RR-P3HT-PCBM complexes caused by the hexyl chains. Thus, these geometries can be excluded from the major CS conformations effectively generated via the CT complexes. For the RRA-P3HT:PCBM blend, the several conformations of $(\alpha, \beta) = (0^\circ, 18^\circ)$, $(-90^\circ, 20^\circ)$, $(-45^\circ, 18^\circ)$, $(45^\circ, -18^\circ)$ and $(90^\circ, -20^\circ)$ are obtained to fit the TREPR data in Tables 1. These angles are exactly the same as the PCBM^{•-} orientations obtained in the RR-P3HT:PCBM system (Table 1), demonstrating that the distant CS states are also produced via the CT complexes generated by the strong π - π stacking interaction between the PCBM and the single-chain P3HT molecules.

In the present analysis, it is assumed that a defined geometry exists for the position and the orientation (D , θ , ϕ , and β) of the PCBM^{•-} molecule with respect to P3HT^{•+} in the radical pairs, as shown in Figure 5 and Table 1, although the distributions are allowed for α and γ because of $g_x \approx g_y$. In the present BHJ blend systems, however, it is likely that there would be a positional distribution in the CS states. On the basis of Conformation I, we have calculated the TREPR spectra for different geometries of $\theta = 50^\circ$ and $\theta = 70^\circ$ in the RR-P3HT:PCBM system at $t = 0.5$ μ s and summed these spectra. The resultant spectrum (not shown) is very close to the calculated spectrum (red line in Figure 2b) using $\theta = 60^\circ$ in Table 1. Therefore, there may exist geometrical distributions around $\theta = 60^\circ$ in the RR-P3HT:PCBM and around $\theta = 75^\circ$ in the RRA-P3HT:PCBM. The distributions may exist as well for the other angles of ϕ and β and for the D value. Such distribution is coincident with the fast transverse relaxation time of $T_2 = 15$ ns in Table 1, as detailed below. However, the predominant single-exponential decay of the thermal equilibrium signal in Figure 3 denotes that the detected CS states of P3HT^{•+}-PCBM^{•-} possess similar molecular geometries so that the positional distributions should not be very large. Thus, it is considered that the majority of the interfacial CS states hold the defined stacking structures so that the hexagonal or pentagonal aromatic rings at the PCBM bottom face the aromatic planes of P3HT.^{4,13,15}

Orbital Characterizations for the Distant Charge-Separation. In Table 1, the positive $2J$ values are explained by the charge-transfer interaction (J_{CT}) by which the S-T energy gap is generated though the configuration interaction from the charge-recombined states.^{33,55,56} In the case that the triplet CR is the predominant deactivation process of the CS state, as detailed in the Supporting Information, the exchange coupling has been approximated as $2J = |V|^2/\Delta E_{CR}$ where $|V|$ and ΔE_{CR} are the electronic coupling matrix element and the vertical energy gap for the CR, respectively.⁵⁵ Because $\Delta G_{CR} = 0$ eV is evaluated as the free energy change for the triplet CR in the Supporting Information, ΔE_{CR} is dominated by the reorganization energy for the CR. From the reported solvent reorganization energy of $\lambda_s = 0.11$ eV and the internal reorganization energy of $\lambda_v = 0.27$ eV,¹³ the total reorganization energy is estimated to be 0.4 eV, resulting in $\Delta E_{CR} = 0.4$ eV. From $2J = 16.0$ μ T in Table 1, $|V| = 0.2$ cm⁻¹ can thus be determined for the CS state in Figure 5. This value of the V is consistent with the triplet CR kinetics determined in Table 1 as follows:

According to the Marcus theory,⁵⁷ the CR rate constant k_{CRT} is represented as follows

$$k_{CRT} = \frac{2\pi}{h} |V|^2 \frac{1}{\sqrt{4\pi\lambda_s k_B T}} \sum_i F C_i \exp \left\{ -\frac{(\lambda_s + \Delta G_{CR} + i h \nu_{vib})^2}{4\lambda_s k_B T} \right\} \quad (5)$$

with

$$F C_i = \exp(-S) \frac{S^i}{i!}, \quad S = \frac{\lambda_v}{h \nu_{vib}} \quad (6)$$

where ν_{vib} , λ_s , λ_v , and ΔG_{CR} represent the vibrational frequency of the stretching bond associated with the intramolecular structural change by the electron transfer, the solvent reorganization energy, the intramolecular reorganization

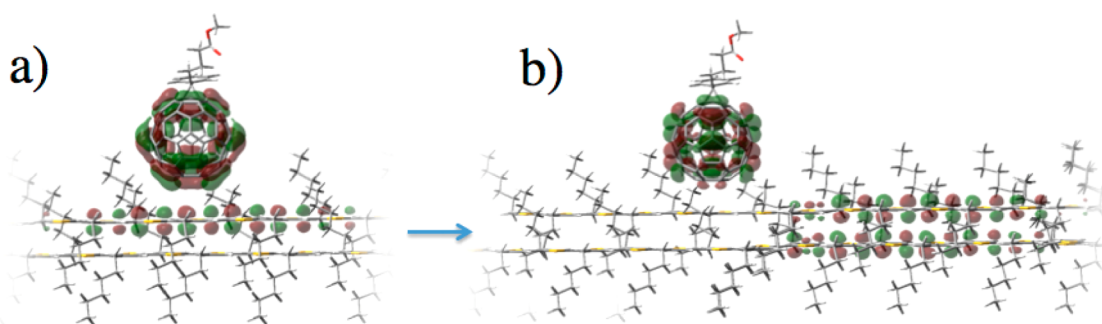


Figure 6. Schematic view of the primary hole dissociation mechanism by the electron–phonon coupling from (a) the photoinduced contact CT state to (b) the delocalized CS state (Figure 5) at the RR-P3HT:PCBM interface at 77 K. In panel a, LUMO+1 is represented as the dominant electron-accepting orbital in PCBM to form the contact CT state possessing the large orbital overlap and the large Coulomb stabilization.

energy, and the driving force for the CR, respectively. With taking into account $h\nu_{\text{vib}} = 1500 \text{ cm}^{-1}$ as the C=C stretching frequency¹³ in the PCBM and in the P3HT, $k_{\text{CRT}} = 3 \times 10^5 \text{ s}^{-1}$ is obtained by substituting $|V| = 0.2 \text{ cm}^{-1}$, $\lambda_{\text{S}} = 0.11 \text{ eV}^{13}$, $-\Delta G_{\text{CR}} = 0.0 \text{ eV}$ (for the triplet CR as described in the Supporting Information), $\lambda_{\text{v}} = 0.27 \text{ eV}^{13}$ and $T = 77 \text{ K}$. Thus, the weak electronic coupling of $|V| = 0.2 \text{ cm}^{-1}$ characterized by the exchange coupling in the RR-P3HT:PCBM system is quantitatively consistent with the small CR rate constant of $4.2 \times 10^5 \text{ s}^{-1}$ in Table 1. Furthermore, in Table 1, the larger J value (28 mT) is obtained for the RRa-P3HT:PCBM system with comparing to the RR-P3HT:PCBM system. This 3.5 times larger J in the RRa-P3HT:PCBM system is in line with the 3.3 times larger CR rate constant of $1.4 \times 10^6 \text{ s}^{-1}$ (Table 1) in the RRa-P3HT:PCBM system than in the RR-P3HT:PCBM system experimentally determined by the TREPR data. This is because the differences both in the exchange coupling and in the CR rate constant are governed by the difference in the square of the electronic coupling of $|V|$ in eq 5.³¹ Therefore, the above electronic coupling determination of $|V| = 0.2 \text{ cm}^{-1}$ and the exchange coupling of $8 \mu\text{T}$ are reasonable for the RR-P3HT:PCBM. $|V| = 0.4 \text{ cm}^{-1}$ is thus estimated for the RRa-P3HT:PCBM system from Table 1.

In the RR-P3HT:PCBM, the small electronic interaction of $|V| = 0.2 \text{ cm}^{-1}$ between the unpaired electronic orbitals (Figure 5) could be explained by a combination of (1) the relatively orthogonal orbital conformations between the SOMOs, as shown in Figure 5b, and (2) the highly delocalized hole distribution not only in the intrachain direction but also in the interchain direction. The latter argument of (2) is well-supported by the larger $|V|$ value (0.4 cm^{-1}) in the RRa-P3HT:PCBM system in which the interchain hole-delocalization does not occur due to the lack of the self-organization structures in the P3HT domains. The quite small electronic interaction in Figure 5 is in sharp contrast with the reported electronic couplings of $\sim 100 \text{ cm}^{-1}$ for the ultrafast charge-injection dynamics from $^1\text{P3HT}^*$ to PCBM.¹³ Looking at the nanostructure of the P3HT-PCBM complex in Figure 5, the difference in the $|V|$ is interpreted by the extreme decrease in the orbital overlap by the initial hole delocalization and dissociation, that is, the nanometer-scale photocurrent generations via the contact CT (Figure 6). In the contact CT state, the larger orbital overlap is expected when the electron-accepting orbital of PCBM employs the next upper orbital (LUMO+1)¹³ to the LUMO because the electron density is highly distributed at the PCBM bottom in the vicinity of the P3HT surface, as shown in Figure 6a.⁵⁰ Also, the initial orbital

distribution of the hole should be localized near the PCBM bottom in the contact CT to yield the large orbital overlap ($V \approx 100 \text{ cm}^{-1}$) by the π -stacking structure.¹³ This situation manifests the certain transition dipole moment^{40,58} by the orbital overlap contributing to the optical CT transition.^{15,39} For the photocurrent generations, the hole needs to escape from the strong CT binding, whose energy is reported to be 0.4 eV^2 . Such dissociation is energetically feasible by switching the unpaired orbitals (as shown in Figure 6) using (1) the delocalization¹⁷ of the interchain hole distribution via the lamellae stacking in P3HT and (2) the internal conversion of the active singly occupied molecular orbital (SOMO) from the LUMO+1 to the LUMO in PCBM.⁵⁰ In the former, the stabilization energy by creating the interchain-polaron from the highest occupied molecular orbital (HOMO) of the single-chain P3HT is estimated to be ca. 0.3 eV by using the polaron absorption spectrum of the RR-P3HT film.⁴⁵ Because of the SOMO switching from LUMO+1 to LUMO in PCBM, the orbital stabilization occurs by 0.05 eV^{13} . Therefore, the total enthalpy change is estimated to be $\Delta H_{\text{orbit}} = -0.4 \text{ eV}$ by the orbital switching from Figure 6a to Figure 6b.

Because the electron density is spherically distributed along the equatorial positions in the LUMO, it is expected from Figure 5b that the rotations of $\text{PCBM}^{\bullet-}$ about the g_z axis by the γ parameter do not produce differences in the orbital overlap between $\text{P3HT}^{\bullet+}$ and $\text{PCBM}^{\bullet-}$, resulting in the dominant single-exponential CR decay (Figure 3) determined by $|V| = 0.2 \text{ cm}^{-1}$ in eq 5. Thus, the single-exponential decay in Figure 3 does not conflict with the arbitrary distributions in α and γ by the amorphous environment at the domain boundaries, as considered in the present materials.

Roles of Phonon on the Primary Hole-Dissociation.

From $\theta = 60^\circ$, the initial molecular photocurrent in Figure 6 is mainly created via the intrachain mobility in P3HT to result in the distant CS state. This preference of the intrachain direction is associated with a coupling of the hole to librations (phonon) of the chains in the conjugated polymer because the coupling is known to contribute to the 1D diffusion of the polaron in the blend materials.⁵⁹ Thus, such an electron–phonon (EP) coupling induces not only the hole motilities^{60,61} but also the spin relaxations.⁵⁹ As listed in Table 1, the spin–lattice relaxation time (T_1) of the distant CS state is determined to be $0.5 \mu\text{s}$ at 77 K. This value is 10 times smaller than $T_1 = 5 \mu\text{s}$ reported for a distant CS state of a zinc porphyrin–fullerene-linked dyad molecule in a frozen solution (91 K).³¹ Also, $T_1 = 0.5 \mu\text{s}$ in Table 1 is smaller than $T_1 = 1 \mu\text{s}$ obtained for a distant CS state ($\text{ZnP}^{\bullet+}\text{--H}_2\text{P--C}_{60}^{\bullet-}$) of a zinc porphyrin-free base

porphyrin–fullerene triad in benzonitrile at room temperature.⁵¹ The unusually fast spin–lattice relaxation in the present system even at 77 K is thus explained by the effective 1D librations by the EP coupling.⁵⁹ Moreover, the phase memory time of 15 ns in Table 1 is similar to the reported T_2 (30 ns)⁴¹ of the free polarons in the P3HT:PCBM blends at 77 K. Such fast transverse relaxation strongly denotes that although the transient CS states possess the conformational structures originating from the ordered π -stackings in Figure 5b, the electronic orbital is fluctuated due to the EP coupling, contributing to the distributed D , J , and angle parameters to affect the T_2 . These fast spin relaxation parameters are consistent with the anticipated distributions in the angle θ , as described above. The pseudorotational mobility in PCBM has also been explained by the phonon-assisted hopping and may play a role for the small T_1 and T_2 in Table 1.^{13,59}

One reviewer has commented that the short T_1 could be caused by the influence of the escaped free radicals from the CR deactivations, as detected in Figure 2e. From the irradiated laser power ($\sim 5 \text{ mJ cm}^{-2}$) per pulse and the effective thickness ($\sim 200 \text{ nm}$) of the blend material that absorbs the 532 nm photons, the density (n) of the escaped radical is estimated to be an order of 10^{19} cm^{-3} , assuming that ca. 5 % of the irradiating photons are converted¹⁵ to the escaped carriers at 77 K. From the temperature dependence of the hole motilities (μ) detected by the time-of-flight technique,²⁵ $\mu < 10^{-7} \text{ cm}^2 \text{ V}^{-1} \text{ s}^{-1}$ is estimated at 77 K for the P3HT:PCBM blend film, leading to the 3D diffusion coefficient ($D_r = \mu k_B T / e$ estimated by the Einstein's relation) to be $D_r < 10^{-8} \text{ cm}^2 \text{ s}^{-1}$ for the free polarons. The diffusion-controlled collision rate constant (k_d) by the free carriers is thus estimated to be $k_d = 4\pi D_r r_{CC} < 10^{-14} \text{ cm}^2 \text{ s}^{-1}$. Therefore, the rate for the free radicals to collide with the transient CS state is estimated to be $k_d n < 10^5 \text{ s}^{-1}$, denoting a very slow fluctuation in the magnetic interaction by the free carriers at 77 K. Such quite slow 3D mobility by the free radicals is consistent with the observations of the anisotropic g -factors by the high-field EPR technique at 77 K.²⁸ The above argument strongly supports that the fast spin relaxations in the CS state are not from the influence of the existing free radical but from the inherent 1D mobility¹⁴ of the hole to produce the distant CS state in Figure 6 by the EP couplings.

From the above results, one can conclude that the molecular motions of the CS state play the second energy-stabilization role for the carrier dissociations, that is, the entropy effect.² When the orbital distribution is delocalized, there may exist a number of local vibrational modes that couple to the hole. It is moreover considered that when the Coulomb attraction is strong enough in Figure 6a the libration will be inhibited because the RR-P3HT⁺• surface is bound to PCBM[−]•. In the case of Figure 6b, the CS states become free from the binding to enhance the degree of freedom by the nuclear motions resulting in the short spin relaxation times.⁵⁹ Such enhanced libration should significantly contribute to the increase (ΔS) in the entropy promoting the initial hole-dissociation as the exothermic process with the free energy change of $-T\Delta S$. Now, one can approximate that the number (W) of the libration states at low temperature is equal to the number of the vibrational modes that couple to the unpaired orbitals in Figure 6. Therefore, W is approximated to be $3N - 6$, where N is the number of the atoms inside the lattice including the orbital in Figure 5 to affect the EP coupling by the organized molecules. When $N \approx 10^4$ is assumed, as an example, one obtains $\Delta S = k_B \ln W \approx 10 k_B$, where k_B is the Boltzmann constant. Using

$\Delta H_{\text{orbit}} = -0.4 \text{ eV}$ estimated above and with $T\Delta S = k_B T \ln W \approx 0.1 \text{ eV}$, the Gibbs free energy change (ΔG_{HD}) for the initial hole dissociation in Figure 6 is expressed as

$$\Delta G_{\text{HD}} = \Delta H_{\text{orbit}} + \Delta H_C - T\Delta S \approx -0.1 \text{ eV} \quad (7)$$

where ΔH_C is the destabilization energy ($\Delta H_C = 0.4 \text{ eV}$) by the weakened Coulomb binding by the hole dissociation. It should be noted that even though the Coulomb binding energy much larger than the thermal energy ($k_B T$) looks hard to overcome, the stabilizations occur by ΔH_{orbit} and by $-T\Delta S$ to compensate the destabilization, resulting in the effective carrier dissociation as the exothermic process.

From the above entropy roles by the molecular motions and from the experimentally characterized geometries (Table 1) of the CS states distributed around the defined center-to-center distances ($r_{CC} = 1.8$ and 1.1 nm for the RR-P3HT:PCBM and the RRA-P3HT:PCBM, respectively), it is considered that the efficiency of the CS-state generation at a distance is determined by a balance between the forces of the entropy and the Coulomb attraction; when the molecular motions are highly effective not only in the intrachain direction but also in the interchain direction, the more distant CS for the direction of $\theta = 60^\circ$ is achieved, overcoming the strong Coulomb attraction at closer distance as in the RR-P3HT:PCBM system at 77 K (Figure 5). Analysis of temperature dependence of the CS geometry is now in progress to clarify the role of the entropy on the carrier dissociations on the nanometer scales.

CONCLUSIONS

Using the TREPR method, the orbital delocalization by the phonon has been shown to play key roles both on the enthalpy and on the entropy for the initial photocurrent generation. At higher temperature, the more effective librations will contribute to the further delocalization around the D/A interface not only in the P3HT domain but also in the PCBM clusters. Thereby, it is strongly anticipated that the more distant and delocalized CS states are exothermically generated from the contact CT, leading to the effective photocurrent generations with the inhibited CRs. This well explains the several reported observations that the quite higher IPCE have been obtained in the organic solar cells at higher temperature than 77 K.¹⁵ In conclusion, the present TREPR study has demonstrated that the structure and spin-relaxation parameters of the transient CS states are useful to characterize the underlying mechanism and function of the initial molecular photocurrent generations by the OPV interfaces. Evidently, the control of the entropy determined by the polymer structure and by the morphology should be the key for the molecular design and the development for the more highly efficient OPV devices.

ASSOCIATED CONTENT

Supporting Information

Details of the computation method, the parameter settings, and the effect of the geometry on the TREPR spectrum. The energetics of the CT and CS states are also presented. This material is available free of charge via the Internet at <http://pubs.acs.org>.

AUTHOR INFORMATION

Corresponding Author

*E-mail: sykobor@ipc.shizuoka.ac.jp.

Notes

The authors declare no competing financial interest.

■ ACKNOWLEDGMENTS

We thank Prof. Hisao Murai (Shizuoka University) and Mr. Hiroto Nagata (Sekisui Nano Coat Technology, Co. Ltd.) for experimental supports and useful discussions. Y.K. thanks Prof. Hideo Ohkita (Kyoto University) and Prof. Kazuhiro Marumoto (Tsukuba University) for helpful suggestions. This work was supported by a Grant-in-Aid for Scientific Research (No. 22550009) from Ministry of Education, Culture, Sports, Science and Technology, Japan. This research was partially carried out by using an instrument at the Center for Instrumental Analysis of Shizuoka University.

■ REFERENCES

- (1) Campoy-Quiles, M.; Ferenczi, T.; Agostinelli, T.; Etchegoin, P. G.; Kim, Y.; Anthopoulos, T. D.; Stavrinou, P. N.; Bradley, D. D. C.; Nelson, J. *Nat. Mater.* **2008**, *7*, 158–164.
- (2) Clarke, T. M.; Durrant, J. R. *Chem. Rev.* **2010**, *110*, 6736–6767.
- (3) Kim, J. Y.; Lee, K.; Coates, N. E.; Moses, D.; Nguyen, T.-Q.; Dante, M.; Heeger, A. J. *Science* **2007**, *317*, 222–225.
- (4) Bakulin, A. A.; Rao, A.; Pavelyev, V. G.; van Loosdrecht, P. H. M.; Pshenichnikov, M. S.; Niedzialek, D.; Cornil, J.; Beljonne, D.; Friend, R. H. *Science* **2012**, *335*, 1340–1344.
- (5) Kim, Y.; Cook, S.; Tuladhar, S. M.; Choulis, S. A.; Nelson, J.; Durrant, J. R.; Bradley, D. D. C.; Giles, M.; McCulloch, I.; Ha, C. S.; et al. *Nat. Mater.* **2006**, *5*, 197–203.
- (6) Mihailetschi, V. D.; Xie, H. X.; de Boer, B.; Koster, L. J. A.; Blom, P. W. M. *Adv. Funct. Mater.* **2006**, *16*, 699–708.
- (7) Deibel, C.; Strobel, T.; Dyakonov, V. *Adv. Mater.* **2010**, *22*, 4097–4111.
- (8) Tada, A.; Geng, Y. F.; Wei, Q. S.; Hashimoto, K.; Tajima, K. *Nat. Mater.* **2011**, *10*, 450–455.
- (9) Li, G.; Shrotriya, V.; Huang, J. S.; Yao, Y.; Moriarty, T.; Emery, K.; Yang, Y. *Nat. Mater.* **2005**, *4*, 864–868.
- (10) Gunes, S.; Neugebauer, H.; Sariciftci, N. S. *Chem. Rev.* **2007**, *107*, 1324–1338.
- (11) Tsoi, W. C.; James, D. T.; Kim, J. S.; Nicholson, P. G.; Murphy, C. E.; Bradley, D. D. C.; Nelson, J.; Kim, J.-S. *J. Am. Chem. Soc.* **2011**, *133*, 9834–9843.
- (12) Guo, J. M.; Ohkita, H.; Bente, H.; Ito, S. *J. Am. Chem. Soc.* **2010**, *132*, 6154–6164.
- (13) Liu, T.; Troisi, A. *J. Phys. Chem. C* **2011**, *115*, 2406–2415.
- (14) Grzegorzczak, W. J.; Savenije, T. J.; Dykstra, T. E.; Pires, J.; Schins, J. M.; Siebbeles, L. D. A. *J. Phys. Chem. C* **2010**, *114*, 5182–5186.
- (15) Lee, J.; Vandewal, K.; Yost, S. R.; Bahlke, M. E.; Goris, L.; Baldo, M. A.; Manca, J. V.; Van Voorhis, T. *J. Am. Chem. Soc.* **2010**, *132*, 11878–11880.
- (16) Ko, S. W.; Hoke, E. T.; Pandey, L.; Hong, S. H.; Mondal, R.; Risko, C.; Yi, Y. P.; Noriega, R.; McGehee, M. D.; Bredas, J. L.; et al. *J. Am. Chem. Soc.* **2012**, *134*, 5222–5232.
- (17) Murthy, D. H. K.; Gao, M.; Vermeulen, M. J. W.; Siebbeles, L. D. A.; Savenije, T. J. *J. Phys. Chem. C* **2012**, *116*, 9214–9220.
- (18) Veldman, D.; Ipek, O.; Meskers, S. C. J.; Sweelssen, J.; Koetse, M. M.; Veenstra, S. C.; Kroon, J. M.; van Bavel, S. S.; Loos, J.; Janssen, R. A. J. *J. Am. Chem. Soc.* **2008**, *130*, 7721–7735.
- (19) Pensack, R. D.; Guo, C.; Vakhshouri, K.; Gomez, E. D.; Asbury, J. B. *J. Phys. Chem. C* **2012**, *116*, 4824–4831.
- (20) Keivanidis, P. E.; Clarke, T. M.; Lilliu, S.; Agostinelli, T.; Macdonald, J. E.; Durrant, J. R.; Bradley, D. D. C.; Nelson, J. *J. Phys. Chem. Lett.* **2010**, *1*, 734–738.
- (21) Sirringhaus, H.; Brown, P. J.; Friend, R. H.; Nielsen, M. M.; Bechgaard, K.; Langeveld-Voss, B. M. W.; Spiering, A. J. H.; Janssen, R. A. J.; Meijer, E. W.; Herwig, P.; et al. *Nature* **1999**, *401*, 685–688.
- (22) Kayunkid, N.; Uttiya, S.; Brinkmann, M. *Macromolecules* **2010**, *43*, 4961–4967.
- (23) Lan, Y.-K.; Huang, C.-I. *J. Phys. Chem. B* **2009**, *113*, 14555–14564.
- (24) Dag, S.; Wang, L.-W. *J. Phys. Chem. B* **2010**, *114*, 5997–6000.
- (25) Mauer, R.; Kastler, M.; Laquai, F. *Adv. Funct. Mater.* **2010**, *20*, 2085–2092.
- (26) Woo, C. H.; Thompson, B. C.; Kim, B. J.; Toney, M. F.; Frechet, J. M. J. *J. Am. Chem. Soc.* **2008**, *130*, 16324–16329.
- (27) Campoy-Quiles, M.; Kanai, Y.; El-Basaty, A.; Sakai, H.; Murata, H. *Org. Electron.* **2009**, *10*, 1120–1132.
- (28) Poluektov, O. G.; Filippone, S.; Martin, N.; Sperlich, A.; Deibel, C.; Dyakonov, V. *J. Phys. Chem. B* **2010**, *114*, 14426–14429.
- (29) Hore, P. J.; Hunter, D. A.; McKie, C. D.; Hoff, A. J. *Chem. Phys. Lett.* **1987**, *137*, 495–500.
- (30) van der Est, A.; Prisner, T.; Bittl, R.; Fromme, P.; Lubitz, W.; Mobius, K.; Stehlik, D. *J. Phys. Chem. B* **1997**, *101*, 1437–1443.
- (31) Kobori, Y.; Fuki, M.; Murai, H. *J. Phys. Chem. B* **2010**, *114*, 14621–14630.
- (32) Prisner, T. F.; van der Eest, A.; Bittl, R.; Lubitz, W.; Stehlik, D.; Mobius, K. *Chem. Phys.* **1995**, *194*, 361–370.
- (33) Kobori, Y.; Fuki, M. *J. Am. Chem. Soc.* **2011**, *133*, 16770–16773.
- (34) Till, U.; Klenina, I. B.; Proskuryakov, I. I.; Hoff, A. J.; Hore, P. J. *J. Phys. Chem. B* **1997**, *101*, 10939–10948.
- (35) Franco, L.; Ruzzi, M.; Corvaja, C. *J. Phys. Chem. B* **2005**, *109*, 13431–13435.
- (36) Behrends, J.; Sperlich, A.; Schnegg, A.; Biskup, T.; Teutloff, C.; Lips, K.; Dyakonov, V.; Bittl, R. *Phys. Rev. B* **2012**, *85*, 125206.
- (37) Uvarov, M.; Kulik, L. *Appl. Magn. Reson.* **2012**, *1*–10.
- (38) Chu, C. W.; Yang, H. C.; Hou, W. J.; Huang, J. S.; Li, G.; Yang, Y. *Appl. Phys. Lett.* **2008**, *92*, 103306.
- (39) Tvingstedt, K.; Vandewal, K.; Gadisa, A.; Zhang, F. L.; Manca, J.; Inganas, O. *J. Am. Chem. Soc.* **2009**, *131*, 11819–11824.
- (40) Imahori, H.; Tkachenko, N. V.; Vehmanen, V.; Tamaki, K.; Lemmetyinen, H.; Sakata, Y.; Fukuzumi, S. *J. Phys. Chem. A* **2001**, *105*, 1750–1756.
- (41) Krinichnyi, V. I.; Yudanov, E. I.; Spitsina, N. G. *J. Phys. Chem. C* **2010**, *114*, 16756–16766.
- (42) Closs, G. L.; Forbes, M. D. E.; Norris, J. R. *J. Phys. Chem.* **1987**, *91*, 3592–3599.
- (43) Kandrashkin, Y.; van der Est, A. *Spectrochim. Acta, Part A* **2001**, *57*, 1697–1709.
- (44) Kothe, G.; Weber, S.; Ohmes, E.; Thurnauer, M. C.; Norris, J. R. *J. Phys. Chem.* **1994**, *98*, 2706–2712.
- (45) Jiang, X. M.; Österbacka, R.; Korovyanko, O.; An, C. P.; Horovitz, B.; Janssen, R. A. J.; Vardeny, Z. V. *Adv. Funct. Mater.* **2002**, *12*, 587–597.
- (46) Zeidan, T. A.; Carmeli, R.; Kelley, R. F.; Wilson, T. M.; Lewis, F. D.; Wasielewski, M. R. *J. Am. Chem. Soc.* **2008**, *130*, 13945–13955.
- (47) Fukuj, T.; Yashiro, H.; Maeda, K.; Murai, H. *Chem. Phys. Lett.* **1999**, *304*, 173–179.
- (48) Watanabe, S.-i.; Tanaka, H.; Kuroda, S.-i.; Toda, A.; Nagano, S.; Seki, T.; Kimoto, A.; Abe, J. *Appl. Phys. Lett.* **2010**, *96*, 173302.
- (49) Zoleo, A.; Maniero, A. L.; Prato, M.; Severin, M. G.; Brunel, L. C.; Kordatos, K.; Brustolon, M. *J. Phys. Chem. A* **2000**, *104*, 9853–9863.
- (50) Kanai, Y.; Grossman, J. C. *Nano Lett.* **2007**, *7*, 1967–1972.
- (51) Kobori, Y.; Yamauchi, S.; Akiyama, K.; Tero-Kubota, S.; Imahori, H.; Fukuzumi, S.; Norris, J. R. *Proc. Natl. Acad. Sci. U. S. A.* **2005**, *102*, 10017–10022.
- (52) Berthold, T.; Gromoff, E. D.; Santabarbara, S.; Stehle, P.; Link, G.; Poluektov, O. G.; Heathcote, P.; Beck, C. F.; Thurnauer, M. C.; Kothe, G. *J. Am. Chem. Soc.* **2012**, *134*, 5563–5576.
- (53) Heinert, U.; Utschig, L. M.; Poluektov, O. G.; Link, G.; Ohmes, E.; Kothe, G. *J. Am. Chem. Soc.* **2007**, *129*, 15935–15946.
- (54) Lilliu, S.; Agostinelli, T.; Pires, E.; Hampton, M.; Nelson, J.; Macdonald, J. E. *Macromolecules* **2011**, *44*, 2725–2734.
- (55) Kobori, Y.; Sekiguchi, S.; Akiyama, K.; Tero-Kubota, S. *J. Phys. Chem. A* **1999**, *103*, 5416–5424.

- (56) Scott, A. M.; Miura, T.; Ricks, A. B.; Dance, Z. E. X.; Giacobbe, E. M.; Colvin, M. T.; Wasielewski, M. R. *J. Am. Chem. Soc.* **2009**, *131*, 17655–17666.
- (57) Marcus, R. A.; Sutin, N. *Biochim. Biophys. Acta* **1985**, *811*, 265–322.
- (58) Gould, I. R.; Young, R. H.; Mueller, L. J.; Albrecht, A. C.; Farid, S. *J. Am. Chem. Soc.* **1994**, *116*, 8188–8199.
- (59) Krinichnyi, V. I.; Yudanov, E. I. *Sol. Energy Mater. Sol. Cells* **2011**, *95*, 2302–2313.
- (60) Cheung, D. L.; McMahon, D. P.; Troisi, A. *J. Phys. Chem. B* **2009**, *113*, 9393–9401.
- (61) Vukmirović, N.; Wang, L. W. *Appl. Phys. Lett.* **2010**, *97*, 043305.